Single-pion production in electron-proton interactions

M. Kabirnezhad*

Department of Physics and Astronomy, York University, 4700 Keele Street, Toronto M3J 1P3, Canada;
University of Oxford, Denys Wilkinson Building, Oxford OX1 3RH, United Kingdom;
and Department of Physics, Imperial College London, London SW7 2BZ, United Kingdom

(Received 29 March 2022; accepted 6 February 2023; published 27 February 2023)

This paper presents an extension of the MK single-pion production model [Kabirnezhad, Phys. Rev. D **97**, 013002 (2018); **102**, 053009 (2020)] to high hadron invariant mass (W) and high momentum transfer (Q^2) to conform to the predictions of perturbative QCD due to the quark-hadron duality evidence. New form factors for several resonances and nonresonant background in the electron-nucleon cross sections are determined taking into account the experimental data and improved evaluation techniques. Fits to electron-proton scattering data are used to constrain free parameters and to assign the related uncertainties of the model. The results from this work can be used to determine the vector current in the corresponding neutrino-nucleon cross sections, which is an important input for event generators in long-baseline neutrino-oscillation measurements.

DOI: 10.1103/PhysRevC.107.025502

I. INTRODUCTION

Neutrino interactions that produce a single pion in the final state are of critical importance to accelerator-based neutrino experiments. Single-pion production (SPP) channels make up the largest fraction of the inclusive neutrino-nucleus cross section in the 1–3 GeV region covered by most accelerator-based neutrino beams. Models of SPP cross-section processes are required to accurately predict the properties of the final state (number of particles and their kinematics) in neutrino interactions. Full predictions incorporate models of the neutrino-nucleon interactions [1–17], models of the nucleus [13,18–22] (in which the target nucleon resides and which must be traversed by the interaction's final-state particles), and models of detector response.

An accurate model for the neutrino-nucleon reaction is essential for an accurate description of neutrino-nucleus interactions. However, a nuclear model is still required to perform comparisons with neutrino-nucleus data. Model comparisons can only test the convolution of nucleon level plus nuclear models. However, if the nucleon level model is known to be accurate, comparison can be used to infer information about the suitability of the nuclear model.

The underlying fundamental theory of SPP from a nucleon is quantum chromodynamics (QCD), and QCD calculations provide important and reliable predictions in the perturbative (high-Q^2) domain. However, in the resonance region (low-Q^2, nonperturbative domain), phenomenological models are necessary to describe SPP. Fortunately, quark-hadron duality [23–25] (which establishes a relationship between the quark-gluon description at high Q^2, and the hadron-meson description at low Q^2) allows for the use of perturbative QCD calculations to constrain the asymptotic (high-Q^2) behavior of form factors in the phenomenological models. Incorporating duality into the model building ensures that the phenomenological constraints from data tend towards the QCD predictions as Q^2 increases.

Most phenomenological models are developed in the low-Q^2 region [$Q^2 < 1.5\,(\mathrm{GeV}/c)^2$] without using the perturbative QCD constraints of the high-Q^2 limit. They include a description of single-pion production through two distinct channels: (i) *resonance production* is where the exchange boson has the requisite four-momentum to excite the target nucleon to a resonance state, which then promptly decays to produce a final-state meson, and (ii) *nonresonant production*, where the pion is created at the interaction vertex (with the outgoing nucleon), which produces final states identical to resonance production that results in non-negligible interference terms.

The majority of SPP models are in quantitative agreement with the experimental data in the first resonance region ($W < 1.3$ GeV) where the resonance structure and the decay amplitude of the Δ resonance are well characterized. However, understanding SPP in the second resonance and the third resonance regions (higher W), where several resonances overlap and interfere with each other, is crucial for neutrino-oscillation experiments such as NOνA and DUNE. The most onerous challenge in developing a high-precision SPP neutrino interaction model is to correctly include the effects of overlapping structures from the many resonances, each with their own form factors, that contribute to the hadronic tensor.

*m.kabirnezhad@imperial.ac.uk

Published by the American Physical Society under the terms of the Creative Commons Attribution 4.0 International license. Further distribution of this work must maintain attribution to the author(s) and the published article's title, journal citation, and DOI. Funded by SCOAP³.

SPP models must contain adjustable parameters associated with each resonance form factor, which can be constrained by data. These parameters from the vector current can be fit to existing electron-scattering data, as discussed in Ref. [2]. However, in this paper, the model is extended to a region with higher Q^2 and W, known as the transition region between resonance and deep-inelastic-scattering (DIS) regions (Sec. II). Therefore, all available electron-scattering SPP data are included in the analysis. We also improved the analysis and the evaluation of the systematic uncertainties, as discussed in Sec. III.

II. THE UPDATE OF THE MK MODEL

The first iteration of the MK model [1,2] provides a full kinematic description of SPP in neutrino-nucleon interactions, including the resonant and the nonresonant interactions plus their interference terms in the helicity basis. In this framework, the cross section is defined (Eq. (18) of Ref. [1]) from the summation of all helicity amplitudes of resonances and nonresonant backgrounds.

The helicity amplitudes are defined by the incident nucleon helicity (λ_1), the outgoing nucleon helicity (λ_2), and the gauge boson's polarization (λ_k):

$$\tilde{F}^{\lambda_k}_{\lambda_2,\lambda_1} = \langle N\pi | e^{\rho}_{\lambda_k} \left(\frac{1}{2M}\right) J^V_{\rho} | N \rangle, \tag{1}$$

where J^V is the hadronic vector current and e_{λ_k} (e_L, e_R, $e_\pm$) are polarizations of the gauge boson (transverse and longitudinal) vectors:

$$e^{\alpha}_{L} = \frac{1}{\sqrt{2}}(0 \quad 1 \quad -i \quad 0),$$

$$e^{\alpha}_{R} = \frac{1}{\sqrt{2}}(0 \quad -1 \quad -i \quad 0),$$

$$e^{\alpha}_{\lambda} = \frac{1}{\sqrt{\left|\left(\epsilon^0_\lambda\right)^2 - \left(\epsilon^3_\lambda\right)^2\right|}}\left(\epsilon^0_\lambda \quad 0 \quad 0 \quad \epsilon^3_\lambda\right),$$

where $\lambda = \mp$ and ϵ^0_λ (ϵ^3_λ) is the first (last) component of the lepton currents:

$$\epsilon^{\rho}_{\lambda} = \bar{u}_{l'_\lambda}(k_2)\gamma^{\rho}(1-\gamma_5)u_l(k_1). \tag{2}$$

The explicit expressions of the helicity amplitude for resonances and nonresonant backgrounds [1,2] are reproduced in Appendixes A and B. The helicity amplitudes of the resonances are a product of the resonance production amplitudes (f^V_{-1}, f^V_{-3}, and $f^{V(\lambda)}_{0+}$) and the decay amplitudes. Resonance production in the MK model [2] follows the Rarita-Schwinger formalism [26] for the first and the second resonance regions ($W < 1.6$ GeV) and the formalisms of the Rein-Sehgal model [4] in the third region ($W > 1.6$ GeV). The nonresonant interactions follow the Hernandez *et al.* model [7], which is deduced from the chiral-perturbation (ChPT) theory Lagrangian of the pion-nucleon system and it is not reliable at high hadron invariant mass ($W > 1.4$ GeV). The vector form factors were defined to improve agreement with exclusive electron-scattering data in the resonance region ($Q^2 < 1\ \mathrm{GeV}/c)^2$.

TABLE I. Vector-meson masses.

k	ρ group	$m_{(\rho)k}$ (GeV)	ω group	$m_{(\omega)k}$ (GeV)
1	$\rho(770)$	0.77526	$\omega(782)$	0.78265
2	$\rho(1450)$	1.465	$\omega(1420)$	1.410
3	$\rho(1700)$	1.720	$\omega(1650)$	1.670
4	$\rho(1900)$	1.885	$\omega(1960)$	1.960
5	$\rho(2150)$	2.149	$\omega(2150)$	2.148

In the updated approach presented here, the MK model is extended to higher momentum transferred (Q^2) by introducing form factors based on vector meson dominance (VMD) models consistent with the QCD theory. The form factors should exhibit a certain asymptotic Q^2 behavior to satisfy the asymptotic condition for helicity amplitudes at $Q^2 \to \infty$, as prescribed by perturbative QCD (pQCD) [23,24].

The VMD model is based on the strongly interacting virtual vector mesons as intermediaries in the coupling between a virtual photon and a nucleon. The model has been a successful theory to determine form factors[1] at low Q^2 and can reproduce Q^2 evolution of form factors at high Q^2, to join smoothly with pQCD calculations [27]. Thus, the VMD models being consistent with pQCD predictions show a satisfactory result in both perturbative and nonperturbative domains [23,28]. A list of vector mesons [23] is shown in Table I.

A. Resonant interactions

The resonance production amplitudes, f^V_{-1}, f^V_{-3}, and $f^{V(\lambda)}_{0+}$, contain the transition nucleon form factors. They are presented in the previous paper [2] and as the electron scattering data is used in this work too. When used in neutrino interactions, the mass of the outgoing charged lepton cannot be ignored for charge current interactions. Therefore, the more general vector helicity amplitudes for the $P_{33}(1232)$, $P_{11}(1440)$, $D_{13}(1520)$, and $S_{11}(1535)$ resonances, which can be used for both electron and neutrino interactions, are presented[2] in Eqs. (3)–(6) (Note that for consistency all the notations in the following relations are taken from the previous works [1,2], such as the nucleon's mass (M), the invariant mass (W), $W_\pm = W \pm M$, $k = k_1 - k_2$, where $k_{1(2)}$ is the momentum of the incoming (outgoing) lepton, $Q^2 = -k^2 = -(k_1 - k_2)^2 = \mathbf{k}^2 - k_0^2$, and $E_k = \sqrt{M^2 + \mathbf{k}^2}$.):

(i) resonance $P_{33}(1232)$

$$f^V_{-3} = -\frac{|\mathbf{k}|}{\sqrt{2W(E_k+M)}}\left[\frac{C_3W_+}{M} + \frac{C_4}{M^2}Wk_0 + \frac{C_5}{M^2}(Wk_0 - k^2)\right],$$

[1]The dipole form factor would be obtained if vector mesons propagate between the virtual photon and the nucleon.

[2]For the rest of the resonances, the helicity amplitudes in the Rein-Sehgal model with the lepton mass correction are used [1,2].

$$f_{-1}^{V} = \frac{|\mathbf{k}|}{\sqrt{6W(E_k+M)}}\left[\frac{C_3}{MW}(k^2 - MW_+) + \frac{C_4}{M^2}Wk_0 + \frac{C_5}{M^2}(Wk_0 - k^2)\right],$$
$$f_{0+}^{V(\lambda)} = -\frac{1}{C_\lambda}\frac{|\mathbf{k}|}{\sqrt{3W(E_k+M)}}\left(|\mathbf{k}|\epsilon_\lambda^0 - k_0\epsilon_\lambda^3\right)\left[\frac{C_3}{M} + \frac{C_4}{M^2}W + \frac{C_5}{M^2}(W - k_0)\right], \quad (3)$$

(ii) resonance $D_{13}(1520)$

$$f_{-3}^{V} = \sqrt{\frac{E_k+M}{2W}}\left[\frac{C_3}{M}W_- + \frac{C_4}{M^2}Wk_0\frac{C_5}{M^2}(Wk_0 - k^2)\right],$$
$$f_{-1}^{V} = \sqrt{\frac{E_k+M}{6W}}\left[\frac{C_3}{M}\left(W_- - 2\frac{\mathbf{k}^2}{E_k+M}\right) + \frac{C_4}{M^2}Wk_0 + \frac{C_5}{M^2}(Wk_0 - k^2)\right],$$
$$f_{0+}^{V(\lambda)} = \frac{1}{C_\lambda}\sqrt{\frac{E_k+M}{3W}}\left(|\mathbf{k}|\epsilon_\lambda^0 - k_0\epsilon_\lambda^3\right)\left[\frac{C_3}{M} + \frac{C_4}{M^2}W + \frac{C_5}{M^2}(W - k_0)\right], \quad (4)$$

(iii) resonance $P_{11}(1440)$

$$f_{-1}^{V} = \frac{|\mathbf{k}|}{\sqrt{W(E_k+M)}}\left[g_1 - \frac{g_2}{W_+^2}k^2\right],$$
$$f_{0+}^{V(\lambda)} = -\frac{1}{C_\lambda}\frac{|\mathbf{k}|}{\sqrt{2W(E_k+M)}}\left(|\mathbf{k}|\epsilon_\lambda^0 - k_0\epsilon_\lambda^3\right) \times \frac{1}{W_+}[g_1 - g_2], \quad (5)$$

(iv) resonance $S_{11}(1535)$

$$f_{-1}^{V} = \sqrt{\frac{(E_k+M)}{W}}\left[\frac{g_1}{W_+^2}k^2 - \frac{g_2}{W_+}W_-\right],$$
$$f_{0+}^{V(\lambda)} = \frac{1}{C_\lambda^V}\sqrt{\frac{E_k+M}{2W}}\left(|\mathbf{k}|\epsilon_\lambda^0 - k_0\epsilon_\lambda^3\right)\left[-\frac{g_1W_-}{W_+^2} + \frac{g_2}{W_+}\right], \quad (6)$$

where the lepton mass appears in $C_\lambda = \sqrt{|(\epsilon_\lambda^0)^2 - (\epsilon_\lambda^3)^2|}$. C_3^V, C_4^V, and C_5^V (g_1^V and g_2^V) are the VMD form factors for resonances with spin-3/2 (spin-1/2). Using the parametrization suggested by Vereshkov and Volchanskiy [23] yields

$$C_\alpha^{(p)}(k^2) = \frac{C_\alpha^{(p)}(0)}{L_\alpha^{(p)}(k^2)}\sum_{k=1}^{K}\frac{a_{\alpha k}m_k^2}{m_k^2 - k^2} \quad (\alpha = 3\text{–}5), \quad (7)$$

$$g_\beta^{(p)}(k^2) = \frac{g_\beta^{(p)}(0)}{L_\beta^{(p)}(k^2)}\sum_{k=1}^{K}\frac{b_{\beta k}m_k^2}{m_k^2 - k^2} \quad (\beta = 1\text{–}2). \quad (8)$$

Here $m_k^2 = m_{(\rho)k}^2$ for the Δ [$P_{33}(1232)$] resonance and $m_k^2 = (m_{(\omega)k}^2 + m_{(\rho)k}^2)/2$ for the resonances in the second region: $P_{11}(1440)$, $D_{13}(1520)$, and $S_{11}(1535)$. Table I gives the masses $m_{(\rho)k}$ and $m_{(\omega)k}$. The logarithmic renormalizations $L_\alpha^{(p)}(k^2)$ and $L_\beta^{(p)}(k^2)$ are defined to retain the asymptotic behavior as it is predicted by pQCD [23]:

$$L_{\alpha(\beta)}^{(p)}(k^2) = \left[1 + h_{\alpha(\beta)}^{(V)}\ln\left(1 - \frac{k^2}{\Lambda_{\rm QCD}^2}\right) + k_{\alpha(\beta)}^{(V)}\ln^2\left(1 - \frac{k^2}{\Lambda_{\rm QCD}^2}\right)\right]^{n_{\alpha(\beta)}/2}, \quad (9)$$

where $n_1 = n_3 \simeq 3$, $n_1 > n_2$, and $n_5 > n_3 > n_4$.

The parameters $a_{\alpha k}$ and $b_{\beta k}$ must obey a number of relations to fulfill asymptotic QCD (quark-hadron duality). They are referred to as *linear superconvergence* relations as discussed in Ref. [23].

For $\alpha = 3$,

$$\sum_{k=1}^{K} a_{3k} = 1, \quad \sum_{k=1}^{K} a_{3k}m_k^2 = 0, \quad \sum_{k=1}^{K} a_{3k}m_k^4 = 0. \quad (10)$$

For $\alpha = 4$ and 5,

$$\sum_{k=1}^{K} a_{\alpha k} = 1, \quad \sum_{k=1}^{K} a_{\alpha k}m_k^2 = 0, \quad \sum_{k=1}^{K} a_{\alpha k}m_k^4 = 0, \quad \sum_{k=1}^{K} a_{\alpha k}m_k^6 = 0. \quad (11)$$

For $\beta = 1$,

$$\sum_{k=1}^{K} b_{1k} = 1, \quad \sum_{k=1}^{K} b_{3k}m_k^2 = 0, \quad \sum_{k=1}^{K} b_{1k}m_k^4 = 0. \quad (12)$$

For $\beta = 2$,

$$\sum_{k=1}^{K} b_{2k} = 1, \quad \sum_{k=1}^{K} b_{2k}m_k^2 = 0, \quad \sum_{k=1}^{K} b_{2k}m_k^4 = 0, \quad \sum_{k=1}^{K} b_{2k}m_k^6 = 0. \quad (13)$$

B. Nonresonant background

The helicity amplitudes of nonresonant backgrounds from the ChPT diagrams were calculated in the previous work [1] and are reproduced in Appendix B. In this work, the dipole vector form factors of ChPT theory (low W) are changed to

VMD form factors as suggested by Lomon [28]. They are

$$
\begin{aligned}
F_1^{iv}(k^2) &= \frac{N}{2}\frac{1.0317+0.0875(1-k^2/0.3176)^{-2}}{1-k^2/0.5496}F_1^{\rho}(k^2)\\
&\quad+\mathcal{R}_{\rho'}\frac{m_{\rho'}^2}{m_{\rho'}^2-k^2}F_1^{\rho}(k^2)\\
&\quad+(1-1.1192N/2-\mathcal{R}_{\rho'})F_1^{D}(k^2),\\
F_2^{iv}(k^2) &= \frac{N}{2}\frac{5.7824+0.3907(1-k^2/0.1422)^{-1}}{1-k^2/0.5362}F_2^{\rho}(k^2)\\
&\quad+\kappa_{\rho'}\mathcal{R}_{\rho'}\frac{m_{\rho'}^2}{m_{\rho'}^2-k^2}F_2^{\rho}(k^2)\\
&\quad+(\kappa_v-6.1731N/2-\kappa_{\rho'}\mathcal{R}_{\rho'})F_2^{D}(k^2),\\
F_1^{is}(k^2) &= \mathcal{R}_{\omega}\frac{m_{\omega}^2}{m_{\omega}^2-k^2}F_1^{\omega}(k^2)\\
&\quad+\mathcal{R}_{\phi}\frac{m_{\phi}^2}{m_{\phi}^2-k^2}F_1^{\phi}(k^2)+(1-\mathcal{R}_{\omega})F_1^{D}(k^2),\\
F_2^{is}(k^2) &= \kappa_{\omega}\mathcal{R}_{\omega}\frac{m_{\omega}^2}{m_{\omega}^2-k^2}F_2^{\omega}(k^2)\\
&\quad+\kappa_{\phi}\mathcal{R}_{\phi}\frac{m_{\phi}^2}{m_{\phi}^2-k^2}F_2^{\phi}(k^2)\\
&\quad\times(\kappa_s-\kappa_{\omega}\mathcal{R}_{\omega}-\kappa_{\phi}\mathcal{R}_{\phi})F_2^{D}(k^2),
\end{aligned}
\tag{14}
$$

where $\kappa_v = 3.793$, $\kappa_s = -0.12$, $m_{\rho'} = 1.465$ GeV, $m_{\omega} = 0.782\,65$ GeV, and $m_{\phi} = 1.020$ GeV. The vector form factors, $F_{1,2}^{\rho}$, $F_{1,2}^{\omega}$, and $F_{1,2}^{D}$, are given by

$$
\begin{aligned}
F_1^{\mathcal{M},D}(k^2) &= \frac{\Lambda_{1,D}^2}{\Lambda_{1,D}^2-\tilde{k}^2}\frac{\Lambda_2^2}{\Lambda_2^2-\tilde{k}^2},\\
F_2^{\mathcal{M},D}(k^2) &= \frac{\Lambda_{1,D}^2}{\Lambda_{1,D}^2-\tilde{k}^2}\left(\frac{\Lambda_2^2}{\Lambda_2^2-\tilde{k}^2}\right)^2,
\end{aligned}
\tag{15}
$$

where $\mathcal{M} = \rho$ and ω and $\Lambda_{1,D}$ is Λ_1 for $F_{1,2}^{\mathcal{M}}$ and Λ_D for $F_{1,2}^{D}$,

$$
\begin{aligned}
F_1^{\phi}(k^2) &= F_1^{\mathcal{M}}\left(\frac{-k^2}{\Lambda_1^2-k^2}\right)^{3/2}, \quad F_1^{\phi}(0)=0,\\
F_2^{\phi}(k^2) &= F_2^{\mathcal{M}}\left(\frac{\mu_{\phi}^2-\Lambda_1^2k^2}{\mu_{\phi}^2\Lambda_1^2-k^2}\right)^{3/2},
\end{aligned}
\tag{16}
$$

where

$$
\tilde{k}^2 = k^2\frac{\ln\left[\left(\Lambda_D^2-k^2\right)/\Lambda_{\rm QCD}^2\right]}{\ln\left(\Lambda_D^2/\Lambda_{\rm QCD}^2\right)}.
$$

The nonresonant background of the MK model is extended to high W ($W > 1.4$ GeV), using the Regge trajectory approach [29]. The propagators of the t-channel meson exchange ChPT diagrams are replaced by the corresponding Regge propagators (ReChi). The expressions of the Regge propagators for the meson trajectories of the π and ρ are the following:

$$
\begin{aligned}
\mathcal{P}_{\pi}(t,s) &= -\alpha_{\pi}'\Gamma[-\alpha_{\pi}(t)]\left(\frac{S}{S_0^{\pi}}\right)^{\alpha_{\pi}(t)},\\
\mathcal{P}_{\rho}(t,s) &= -\alpha_{\rho}'\Gamma[-\alpha_{\rho}(t)]\left(\frac{S}{S_0^{\rho}}\right)^{[\alpha_{\rho}(t)-1]},
\end{aligned}
\tag{17}
$$

where S_0^{π} and S_0^{ρ} are adjustable parameters. The Regge trajectory of π and ρ are as follows:

$$
\begin{aligned}
\alpha_{\pi}(t) &= 0.75\left(t-m_{\pi}^2\right),\\
\alpha_{\rho}(t) &= 0.53+0.85t.
\end{aligned}
\tag{18}
$$

Following the Hybrid model's parametrization [11], the helicity amplitudes for nonresonant background will be

$$
\tilde{F} = \cos^2\phi(W)\tilde{F}_{\rm ChPT}+\sin^2\phi(W)\tilde{F}_{\rm ReChi},
\tag{19}
$$

where $\tilde{F} = \tilde{F}^{\lambda_k}_{\lambda_2,\lambda_1}$ and

$$
\phi(W) = \frac{\pi}{2}\left(1-\frac{1}{\frac{\exp(W-1.7)}{0.1}}\right).
\tag{20}
$$

$\tilde{F}_{\rm ChPT}$ are the helicity amplitudes for the ChPT background and $\tilde{F}_{\rm ReChi}$ are the modified helicity amplitudes with Regge propagators.

This approach with the linear Regge trajectories [Eq. (18)] is valid at high-energy and low-momentum transfer. To ensure that the model reproduces data at high-momentum transfer, the trajectories are multiplied by a factor of $(1+2.4Q^2/W^2)^{-1}$, as suggested in Ref. [30]. The adjustable parameters in the Regge trajectory and VMD form factors are fit to the available exclusive electron-scattering data in the next section.

III. ANALYSIS OF ELECTRON-INDUCED EXCLUSIVE DATA

Exclusive SPP electron-proton-scattering data are used to fit the relevant free parameters of the model. Fits were used to determine the Q^2 dependence of the transition form factors for resonance production and nonresonant background SPP. The analysis method is similar to the previous work [2]. There measurements of the single-pion differential cross sections for electrons scattering off of a hydrogen target in a limited kinematic region [31,32] were used in the fits. However, in this analysis, all available data from the CLAS Collaboration [31–35] in the relevant kinematic region ($Q^2 \in [0.16–6.00]$ $(\mathrm{GeV}/c)^2$ and $W \in [1.1–2.01]$ GeV) were used.

A list of resonances with vector currents, used in this updated MK model, is given in Table II. All resonances are included since data with higher W are included in the fit. Therefore, all resonances in Table II will have their own form factors. This differs from the previous analysis where only data with $W < 1.68$ GeV were included in the fit.

The use of external data to constrain the free parameters of the model has a large impact on the model predictions. It is, therefore, crucial to minimize the bias that would come from a single experiment's measurement via systematic uncertainties or by extrapolating data outside the regions of that

TABLE II. Nucleon resonances, resonance's mass (M_R), resonance's width (Γ_0), branching ratio (χ_E), resonance's signs (σ^D), and resonance's phases.

Resonance	M_R (MeV)	Γ_0 (MeV)	χ_E	σ^D	Phase
$P_{33}(1232)$	1236	130	0.994	+	0.55
$P_{11}(1440)$	1410	423	0.65	+	0.0
$D_{13}(1520)$	1519	120	0.60	+	1.68
$S_{11}(1535)$	1545	175	0.45	−	1.60
$P_{33}(1600)$	1.64	200	0.16	+	1.98
$S_{31}(1620)$	1610	130	0.3	+	–
$F_{15}(1680)$	1685	120	0.65	−	–
$D_{33}(1700)$	1710	300	0.15	+	–
$P_{11}(1710)$	1710	140	0.11	−	–
$P_{13}(1720)$	1720	250	0.11	+	–
$F_{35}(1905)$	1880	330	0.12	−	–
$P_{31}(1910)$	1900	300	0.22	+	–
$P_{33}(1920)$	1920	300	0.12	−	–
$F_{37}(1950)$	1930	285	0.40	+	–

experiment's kinematic coverage. A simultaneous fit to the full dataset properly accounts for correlations in the experimental data. The evaluation provides a covariance matrix for the fit parameters required to fully characterize the systematic uncertainty of the model. By design this matrix properly includes correlations in the data as well as those enforced by the model.

As a practical matter, the addition of several datasets from different channels and kinematic regions can lead to Peelle's Pertinent puzzle [36]. It is likely to occur when a significant discrepancy exists or some experimental uncertainties are unaccounted for or underestimated. As described in Ref. [37], some of the electron-scattering data used in this fit do not have systematic uncertainties evaluated for all angular bins, and in some cases, no systematic uncertainties are reported. In addition, the measurements (see Table III) for the $ep \to en\pi^+$ channel at high Q^2 (or W) have uncertainties lower than those for measurements of other channels. This result tends to favor the data used to constrain these channels noticeably over the $ep \to ep\pi^0$ channel. Therefore, weighting factors are introduced for problematic datasets in order to avoid Peelle's Pertinent puzzle and to reduce any bias to regions not covered by those data. The weighting factors for different datasets used in this analysis are shown in Table III.

TABLE III. Datasets analyzed by the CLAS Collaboration over a vast kinematic range for two channels and their weighting factors (WF) used in this analysis.

Channel	E_e (GeV)	Q^2 (GeV/c)^2	W (GeV)	WF
$ep \to ep\pi^0$	1.046	0.16–0.32	1.1–1.34	0.85
$ep \to en\pi^+$	1.046	0.16–0.32	1.1–1.34	0.5
$ep \to en\pi^+$	1.515	0.30–0.60	1.11–1.57	1
$ep \to ep\pi^0$	1.645	0.40–0.90	1.1–1.68	1
$ep \to ep\pi^0$	2.445	0.65–1.80	1.1–1.68	1
$ep \to en\pi^+$	5.499	1.80–4.00	1.62–2.01	0.5
$ep \to en\pi^+$	5.754	1.72–4.16	1.15–1.67	0.5
$ep \to ep\pi^0$	5.754	3.00–6.00	1.11–1.39	1

TABLE IV. Fit parameters (spin-3/2 resonances). Dependent parameters are tabulated in the lower part of the table.

Parameters	$P_{33}(1232)$	$D_{13}(1520)$
a_{14}^V	−1.4533	−1.410
$C_3^V(0)$	1.98	2.70
$C_4^V(0)$	−1.4285	−2.598
$C_5^V(0)$	0.0	0.883
Λ^V	0.26	0.116
h_3^V	−0.0415	0.1751
k_3^V	0.0216	−0.0338
h_4^V	−0.0642	0.0
k_4^V	0.0341	0.0
h_5^V	–	0.0
k_5^V	–	0.0
a_{11}^V	2.0897	2.3544
a_{12}^V	−3.4146	−4.5682
a_{13}^V	3.7782	4.6238
a_{21}^V	2.101	2.142
a_{22}^V	−3.586	−3.41
a_{23}^V	4.033	3.146
a_{24}^V	−1.548	−0.879

The 88 free parameters cover all 14 transition form factors for resonance production and nonresonant backgrounds. These parameters are fit to the experimental data using the MIGRAD algorithm in the MINUIT2 software package. The best-fit results with a reduced χ^2 of 3.05 are discussed below.

A. VMD form factors for spin-3/2 resonances

There are two spin-3/2 resonances in the first and the second resonance regions, i.e., Δ [$P_{33}(1232)$] and $D_{13}(1520)$, with the form factors given in Eq. (7). According to Ref. [23], the first four mesons in Table I are enough to describe the VMD form factors of the spin-3/2 resonances. Therefore, $K = 4$ in Eq. (7). All the parameters in $a_{\alpha k}$, $\alpha = 4$ and 5, are fixed by the four superconvergence relations in Eq. (11). However, the parameters a_{3k} satisfy three superconvergence relations [Eq. (10)] and only one free parameter remains. The QCD scale in the logarithmic renormalization [Eq. (9)] can vary between $\Lambda_{\rm QCD} \in [0.19\text{–}0.24]$ GeV [23] and $n_{\alpha=3} = 3$, $n_{\alpha=4} = 2$, and $n_{\alpha=5} = 4$. Also, a cutoff form factor is multiplied by the form factor of the Δ resonance, as is suggested in Refs. [30,38]:

$$F(p_\Delta) = \lambda_\Delta^4 / \left[\lambda_\Delta^4 + \left(p_\Delta^2 - M_\Delta^2\right)^2\right], \tag{21}$$

where p_Δ and M_Δ are the mass and the momentum of the Δ resonance and λ_Δ is a free parameter. The λ_Δ parameter and other adjusted parameters related to spin-3/2 resonances are reported in Table IV.

TABLE V. Fit parameters (spin-1/2 resonances). Dependent parameters are tabulated in the bottom part of the table.

Parameters	$P_{11}(1440)$	$S_{11}(1535)$
b_{14}^V	48.8104	−35.7166
b_{15}^V	−15.7527	44.4834
b_{25}^V	9.259 04	−23.5822
$g_1^V(0)$	−0.0597	49.7948
$g_2^V(0)$	44.5325	0.05281
Λ^V	0.1172	0.116
h_1^V	−0.495 84	25.5208
k_1^V	0.064 03	−1.8348
h_2^V	7.3580	−0.7442
k_2^V	−0.5423	0.1412
b_{11}^V	3.1765	−42.9822
b_{12}^V	10.6432	187.041
b_{13}^V	−45.8774	−151.826
b_{21}^V	5.8018	−7.1802
b_{22}^V	−34.9428	76.908
b_{23}^V	61.6342	−145.823
b_{24}^V	−40.7521	100.677

B. VMD form factors for spin-1/2 resonances

There are two spin-1/2 resonances in the second resonance region, i.e., $P_{11}(1440)$ and $S_{11}(1535)$ with the form factors in Eq. (8). Five mesons in Table I are taken into account, as suggested in Ref. [23]. Therefore, $K = 5$ for spin-1/2 resonances. As a result there will be two free parameters in b_{1k} due to the three superconvergence relations [Eq. (12)], and one free parameter will be allowed for b_{2k} due to the four superconvergence relations in Eq. (13). The QCD scale in the logarithmic renormalizations ($L_\beta^{(p)}$) can vary between $\Lambda_{\rm QCD} \in [0.19\text{–}0.24]$ GeV and $n_{\beta=1} = 3$ and $n_{\beta=2} = 2$. All adjusted parameters related to spin-1/2 resonances are reported in Table V.

C. Dipole form factors for resonances in the third region

The characteristic feature of the third region is overlapping structures of several resonances, each with a smaller overall contribution to the hadronic tensor. The Rein-Sehgal model with a simple dipole form factor for each resonance is used to avoid having a relatively large number of parameters (as is done with VMD form factors) in a small phase space. The hadron current of each resonance in the third resonance region was related to a dipole form factor with two adjustable parameters, $F_V(0)$ and M_V:

$$F_V(k^2) = F_V(0)\left(1 - \frac{k^2}{M_V^2}\right)^{-2}\left(1 - \frac{k^2}{M^2}\right)^{n/2}, \qquad (22)$$

where n is the number of oscillators from the Rein-Sehgal model. The number of oscillators and parameters $F_V(0)$ and M_V are reported in Table VI for resonances in the third region.

TABLE VI. Fit result for the third resonance region.

Resonance	$F^V(0)$	M_V (GeV)	n
$P_{33}(1600)$	2.399	1.01	2
$S_{31}(1620)$	0.10	0.10	1
$F_{15}(1680)$	1.362	0.692	2
$D_{33}(1700)$	1.297	0.10	1
$P_{11}(1710)$	0.10	0.10	2
$P_{13}(1720)$	3.00	0.278	2
$F_{35}(1905)$	3.00	1.141	2
$P_{31}(1910)$	3.00	0.697	2
$P_{33}(1920)$	0.10	10.00	2
$F_{37}(1950)$	3.00	0.576	2

TABLE VII. Fit result for nonresonant interactions

Parameters	Best-fit value	Parameters	Best-fit value
$\mathcal{R}_{\rho'}$	−1.358	N	1.20
$\kappa\rho'$	−3.821	$\Lambda_{\rm QCD}$	0.260
$\mathcal{R}_\omega$	0.862	Λ_D	2.111
κ_ω	−49.899	Λ_1	0.841
$\mathcal{R}_\phi$	−7.605	Λ_2	0.419
κ_ϕ	0.081	S_0^π	3.995
μ_ϕ	0.130	S_0^ρ	0.769

D. The VMD form factors for nonresonant interactions

The update for nonresonant interaction was presented in Sec. II B. The adjustable parameters for nonresonant form factors are defined in Eqs. (14)–(16) and the adjustable parameters for Regge propagators are defined in Eq. (17). All parameters related to nonresonant interactions and their best fits are reported in Table VII.

IV. RESULTS AND COMPARISON WITH EXPERIMENTAL DATA

In this section, the fit results from the updated MK model including the 1σ error band are presented. The systematic error band is constructed by randomly throwing the complete set of fit parameters within their post-fit correlated uncertainties (as encoded by the post-fit covariance matrix). The 1σ error on each bin and bib to bin correlations are calculated from the range containing 68% of the throws closest to the best-fit model prediction. The standard cross-section formula for the single-pion electroproduction in the resonance rest frame is the following:

$$\frac{d^5\sigma_{ep\to e'\pi N}}{dE_{e'}d\Omega_{e'}d\Omega_\pi^*} = \Gamma_{\rm em}\left[\frac{d\sigma_T}{d\Omega_\pi^*} + \epsilon\frac{d\sigma_L}{d\Omega_\pi^*} + \sqrt{2\epsilon(1+\epsilon)}\frac{d\sigma_{LT}}{d\Omega_\pi^*}\cos\phi_\pi^* + \epsilon\frac{d\sigma_{TT}}{d\Omega_\pi^*}\cos 2\phi_\pi^* + h_e\sqrt{2\epsilon(1+\epsilon)}\frac{d\sigma_{LT'}}{d\Omega_\pi^*}\sin\phi_\pi^*\right], \qquad (23)$$

where Ω_π^* is the polar and azimuthal pion angles in the resonance rest frame and

$$\Gamma_{\rm em} = \frac{\alpha}{2\pi^2 Q^2}\frac{E_e}{E_{e'}}\frac{q_\gamma}{1-\epsilon} \tag{24}$$

is the virtual photon flux factor with $q_\gamma = (W^2 - M^2)/2M$, and $\epsilon = [1 + 2(q_\gamma^2/Q^2)\tan^2(\delta/2)]^{-1}$ where δ is the scattering angle of electron.

Some SPP models were developed prior to the MK model. They used different theoretical calculations and parametrization, but fit to the same experimental data. They include the following.

(i) Unitary isobar model: MAID2007 [39] is the latest version of unitary isobar model for partial wave analysis on the world data of pion photo- and electroproduction in the resonance region ($Q^2 < 5.0$ $(\mathrm{GeV}/c)^2$).
(ii) Dynamical coupled-channels (DCC) model [9,40–43]: DCC analysis uses the limited pion photo- and electroproduction data ($Q^2 < 3.0$ $(\mathrm{GeV}/c)^2$).
(iii) Hybrid model [11]: Only valid at low Q^2, the Rarita-Schwinger formalism plus Regge approach is used for the resonant and nonresonant interactions like the MK model. However the form factors in the two models are different. The form factors in the hybrid model are from a fit to the MAID result [26].

The selected results, in Figs. 1 and 2, are chosen to show a broad range of Q^2 ($\in$ [0.16–6.00] $(\mathrm{GeV}/c)^2$) and W ($\in$ [1.1–2.01] GeV) for two channels with $p\pi^0$ and $n\pi^+$ final-state hadrons. Note that the valid region for the above models is smaller than that for the MK model. Therefore, the missing results from the above models in Figs. 1–4 are due to the model's stated limitations.

Figure 1 shows the cross section for the $ep \to en\pi^+$ channel and Fig. 2 shows the cross section for the $ep \to ep\pi^0$ channel in terms of the pion polar angle in the resonance rest frame, $\cos\theta^*$. Plots at very low invariant mass ($W < 1.15$ GeV) are dominated by nonresonant background contributions where all models show relatively good agreement with the data. At higher W, the Δ resonance has a dominant contribution in plots with $W \in$ [1.18–1.3 GeV] where the hybrid model deviates from the data above the Δ resonance's peak ($W > 1.23$ GeV) as seen in the second group of plots in Figs. 1 and 2.

At still higher invariant mass of the second resonance region ($W \in$ [1.4–1.6 GeV]), the next three resonances [$P_{11}(1440)$, $D_{13}(1520)$, and $S_{11}(1535)$] dominate. The second group of plots in Fig. 2 shows that the DCC results overestimate the data but the shape agrees with the data. The hybrid model does not predict the backward pion well. It also underpredicts the data in the dip region between the first and the second resonance regions, i.e., $W \in [1.28 - 1.4\,\mathrm{GeV}]$, which is visible in Figs. 1 and 2.

The MAID results [44] show agreement with data at low Q^2 (two top groups of plots in Fig. 1 and 2); however, at higher Q^2, the result favors data from the $ep \to ep\pi^0$ channel over the $ep \to en\pi^+$ channel.

The rest of the resonances in the Table II contribute to the third resonance region ($W > 1.6$ GeV) and only one measurement for the $ep \to en\pi^+$ channel exists. This is presented in the third group of plots in Fig. 1 where the MAID results deviate by more than 3σ from the data.

Some of the datasets in Table III are over a large range of hadron invariant mass which will allow the cross section in different resonance regions to be shown. See Fig. 3 (Fig. 4) for low (medium) Q^2. Comparing the two channels in each figure reveals the different W distributions, which are mainly due to the different Clebsch-Gordan coefficients for isospin-3/2 and -1/2 resonances. The first resonance region is dominant in the $ep \to ep\pi^0$ channel due to larger Clebsch-Gordan coefficients for the Δ (isospin-3/2) resonance. The second resonance region is more pronounced for the $ep \to en\pi^+$ channel because this region is populated mainly by isospin-1/2 resonances that have larger Clebsch-Gordan coefficients for this channel. The isospin Clebsch-Gordan coefficients are given in Table IX.

All comments about the model comparisons in the first and the second resonance regions from Figs. 1 and 2 are visible in Figs. 3 and 4. The third resonance region is not visible here. The DCC prediction for the $ep \to en\pi^+$ channel at low Q^2 and forward pion angles (top plots in Fig. 3) overestimate the data in the second resonance region.

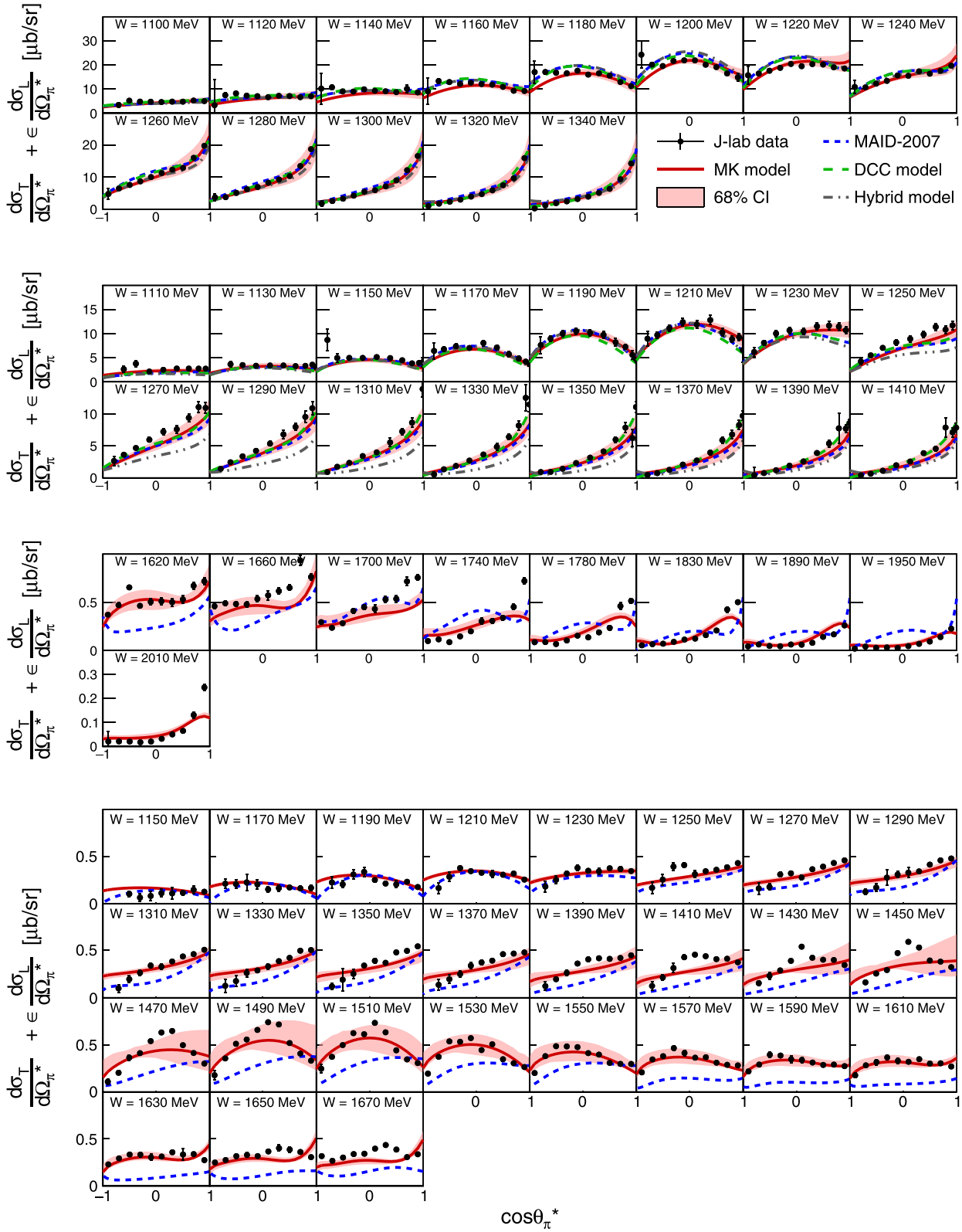


FIG. 1. Data-model comparisons for the $ep \to en\pi^+$ channel at $Q^2 = 0.2$, 0.6, 2.6, and 3.48 $(\mathrm{GeV}/c)^2$, from top to bottom, respectively. The MK model result is the solid red line and the 68% confidence interval is shown by the shaded band. The MAID, DCC and hybrid results are shown by the dashed blue, long-dashed green, and dash-dotted gray lines, respectively.

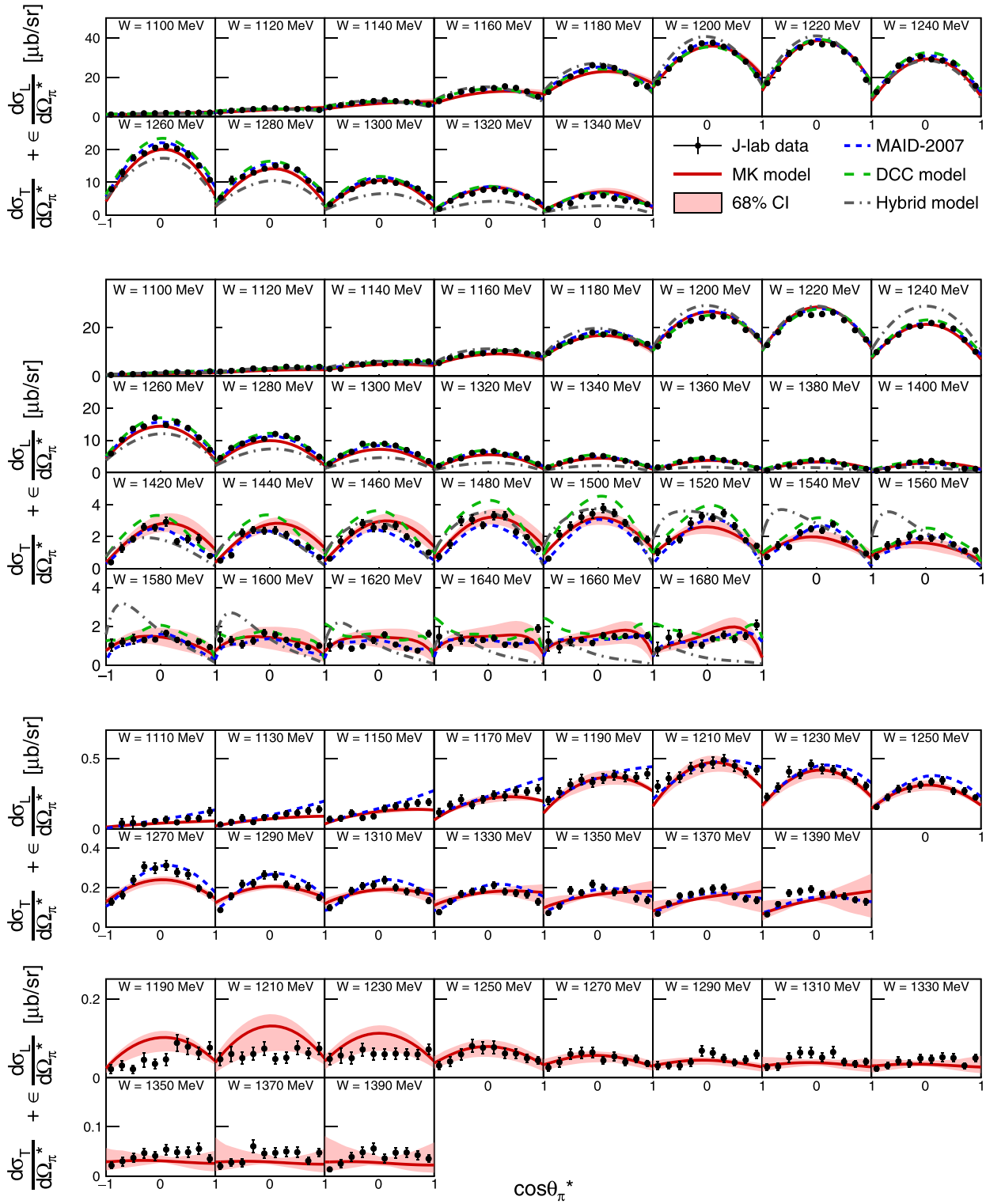


FIG. 2. Data-model comparisons for the $ep \to ep\pi^0$ channel at $Q^2 = 0.16$, 0.4, 3.5, and 6.00 $(\mathrm{GeV}/c)^2$, from top to bottom, respectively. The MK model result is the solid red line and the 68% confidence interval is shown by the shaded band. The MAID, DCC and hybrid results are shown by the dashed blue, long-dashed green, and dash-dotted gray lines, respectively.

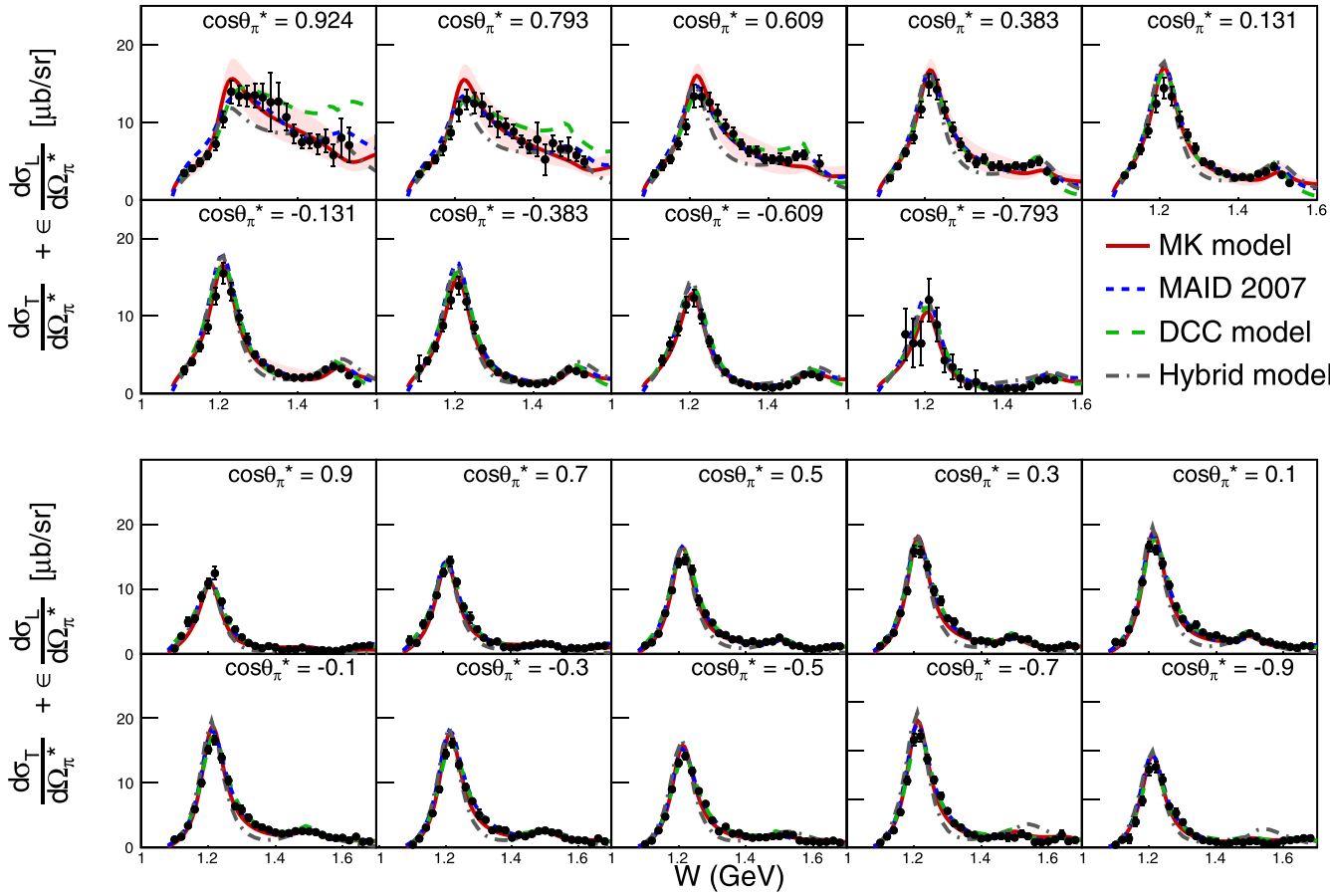


FIG. 3. Data-model comparisons for low Q^2; $Q^2 = 0.4$ (GeV/c)^2 for the $ep \to en\pi^+$ channel (top) and $Q^2 = 0.65$ (GeV/c)^2 for the $ep \to ep\pi^0$ channel (bottom). The MK model result is shown by the solid red line and the 68% confidence interval is shown by the the shaded band. The MAID, DCC, and hybrid results are shown by the dashed blue, long-dashed green, and dash-dotted gray lines, respectively.

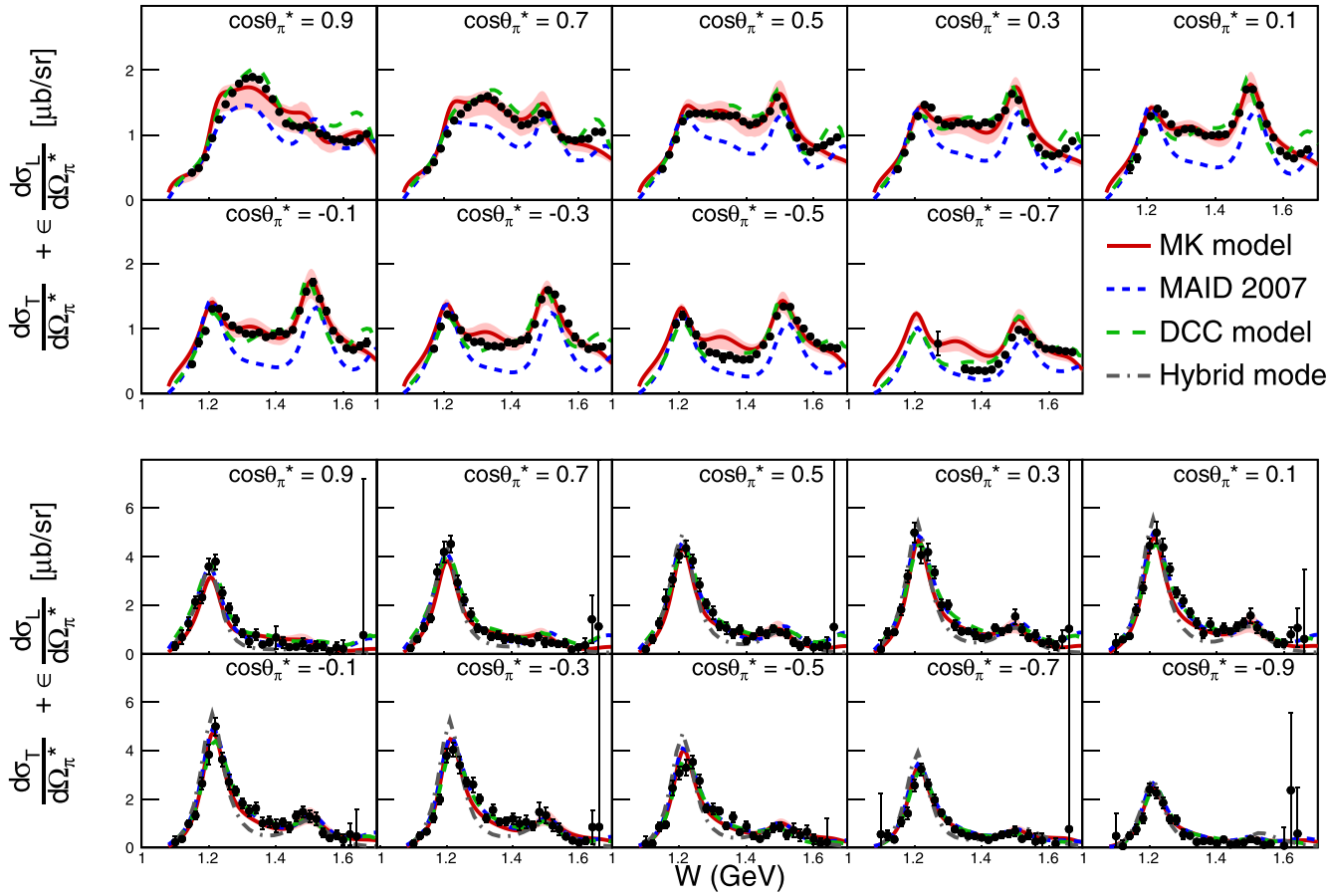


FIG. 4. Data-model comparisons for medium Q^2; $Q^2 = 2.05$ (GeV/c)^2 for the $ep \to epn\pi^+$ channel (top) and $Q^2 = 1.45$ (GeV/c)^2 for the $ep \to ep\pi^0$ channel (bottom). The MK model result is shown by the solid red line and the 68% confidence interval is shown by the shaded band. The MAID, DCC, and hybrid results are shown by the dashed blue, long-dashed green, and dash-dotted gray lines, respectively.

V. CONCLUSION

In this work the vector current description of the MK model is improved by extending the valid region of the model by using all exclusive single-pion electroproduction data and advanced analysis techniques. The MK model is extended to high momentum transfer by using the vector meson dominance form-factor model consistent with the quantum chromodynamics theory through quark-hadron duality. It is also extended to high hadron invariant mass by using Regge phenomenology, i.e., by replacing the t-channel Feynman propagators with the corresponding Regge trajectories.

The free parameters of the model are constructed by fitting to exclusive electron-scattering data in a large kinematic region. The free parameters determine the behaviors of the vector form factors of resonances and the proton in the nonresonant interaction. An advanced analysis method with the improved parametrization produces a systematic uncertainty tied to data and minimizes bias.

The goodness-of-fit and the fit results of the analysis used in defining the MK model (Figs. 1–4) in a broad range of Q^2 ($\in$ [0.16–6.00] $(\mathrm{GeV}/c)^2$) and W ($\in$ [1.1–2.01] GeV) show the resulting nucleon form factors are adequate to describe the data for both channels. The overall agreement with data demonstrates that the VMD model can describe form factors in both perturbative and nonperturbative domains. Therefore, reasonable behavior of the MK model now extends outside the resonant region and into the transition region between the resonance and DIS regions. The results show some disagreements with the data, especially in regions with high Q^2 (see the bottom plots of Fig. 2), but the error bands generally accommodate the disagreements. This feature is of crucial importance to experimental efforts in need of a SPP model.

Other models were also compared with data in their own valid regions. At low Q^2, the data (from both channels) are well described by the MAID model. At higher Q^2, the MAID results show the data agreement for the $ep \to ep\pi^0$ channel is better than that for the $ep \to en\pi^+$ channel. Since in theory the only difference between the two channels is the Clebsch-Gordan coefficients, this demonstrates a bias in their analysis.

The DCC results overestimate data in the second resonance region, but the deviation is small as can be seen in the second group of plots in Fig. 2. However, the model agrees with data in its stated valid region [$Q^2 < 3.0$ $(\mathrm{GeV}/c)^2$]. The hybrid model predictions, which are not a direct fit result to the experimental data, are more than 3σ away from the experimental data, mainly in the second resonance and transition regions.

The hadron currents for resonant and nonresonant interactions from this work will be used in the hadron vector current of the neutrino-nucleon cross sections. The electron-scattering data used in this work covers the kinematic regions essential for all accelerator-based long-baseline neutrino experiments.

ACKNOWLEDGMENTS

I am extremely grateful to Deborah Harris and Dave Wark for being a constant source of encouragement and support. I appreciate the support from my colleagues at Fermilab. I would like to thank the York neutrino group, Stephen Dolan, and Daniel Cherdack for fruitful discussions. I am also thankful to L. Cole Smith, Toru Sato, and Alexis Nikolakopoulos for providing me with data and the model's predictions for single-pion electroproduction. This work was supported by the NSERC and the Royal Commission for the Exhibition of 1851.

TABLE VIII. Vector helicity amplitudes of resonant interaction.

λ_2	λ_1	$\tilde{F}^{e_L}_{\lambda_2\lambda_1}(\theta,\phi)$	$\tilde{F}^{e_R}_{\lambda_2\lambda_1}(\theta,\phi)$
		$\pm\sum_j \frac{2j+1}{\sqrt{2}}\mathcal{D}^j(R)f^V_{-3}\left[R\left(I, j=l\pm\frac{1}{2}\right)\right]d^j_{\frac{3}{2}\frac{1}{2}}(\theta)e^{-2i\phi}$	$-\sum_j \frac{2j+1}{\sqrt{2}}\mathcal{D}^j(R)f^V_{-1}\left[R\left(I, j=l\pm\frac{1}{2}\right)\right]d^j_{\frac{1}{2}-\frac{1}{2}}(\theta)$
$\frac{1}{2}$	$\frac{1}{2}$	$\sum_j \frac{2j+1}{\sqrt{2}}\mathcal{D}^j(R)f^V_{-3}\left[R\left(I, j=l\pm\frac{1}{2}\right)\right]d^j_{\frac{3}{2}-\frac{1}{2}}(\theta)e^{-i\phi}$	$\pm\sum_j \frac{2j+1}{\sqrt{2}}\mathcal{D}^j(R)f^V_{-1}\left[R\left(I, j=l\pm\frac{1}{2}\right)\right]d^j_{\frac{1}{2}\frac{1}{2}}(\theta)e^{i\phi}$
$-\frac{1}{2}$	$\frac{1}{2}$		
$\frac{1}{2}$	$-\frac{1}{2}$	$\mp\sum_j \frac{2j+1}{\sqrt{2}}\mathcal{D}^j(R)f^V_{-1}\left[R\left(I, j=l\pm\frac{1}{2}\right)\right]d^j_{\frac{1}{2}\frac{1}{2}}(\theta)e^{-i\phi}$	$-\sum_j \frac{2j+1}{\sqrt{2}}\mathcal{D}^j(R)f^V_{-3}\left[R\left(I, j=l\pm\frac{1}{2}\right)\right]d^j_{\frac{3}{2}-\frac{1}{2}}(\theta)e^{i\phi}$
$-\frac{1}{2}$	$-\frac{1}{2}$	$-\sum_j \frac{2j+1}{\sqrt{2}}\mathcal{D}^j(R)f^V_{-1}\left[R\left(I, j=l\pm\frac{1}{2}\right)\right]d^j_{\frac{1}{2}-\frac{1}{2}}(\theta)$	$\pm\sum_j \frac{2j+1}{\sqrt{2}}\mathcal{D}^j(R)f^V_{-3}\left[R\left(I, j=l\pm\frac{1}{2}\right)\right]d^j_{\frac{3}{2}\frac{1}{2}}(\theta)e^{2i\phi}$
		$\tilde{F}^{e_-}_{\lambda_2\lambda_1}(\theta,\phi)$	$\tilde{F}^{e_+}_{\lambda_2\lambda_1}(\theta,\phi)$
		$\frac{\lvert\mathbf{k}\rvert}{\sqrt{-k^2}}\sum_j \frac{2j+1}{\sqrt{2}}\mathcal{D}^j(R)f^{V(-)}_{0+}\left[R\left(I, j=l\pm\frac{1}{2}\right)\right]d^j_{\frac{1}{2}\frac{1}{2}}(\theta)e^{-i\phi}$	$\frac{\lvert\mathbf{k}\rvert}{\sqrt{-k^2}}\sum_j \frac{2j+1}{\sqrt{2}}\mathcal{D}^j(R)f^{V(+)}_{0+}\left[R\left(I, j=l\pm\frac{1}{2}\right)\right]d^j_{\frac{1}{2}\frac{1}{2}}(\theta)e^{-i\phi}$
$\frac{1}{2}$	$\frac{1}{2}$	$\pm\frac{\lvert\mathbf{k}\rvert}{\sqrt{-k^2}}\sum_j \frac{2j+1}{\sqrt{2}}\mathcal{D}^j(R)f^{V(-)}_{0+}\left[R\left(I, j=l\pm\frac{1}{2}\right)\right]d^j_{\frac{1}{2}-\frac{1}{2}}(\theta)$	$\pm\frac{\lvert\mathbf{k}\rvert}{\sqrt{-k^2}}\sum_j \frac{2j+1}{\sqrt{2}}\mathcal{D}^j(R)f^{V(+)}_{0+}\left[R\left(I, j=l\pm\frac{1}{2}\right)\right]d^j_{\frac{1}{2}-\frac{1}{2}}(\theta)$
$-\frac{1}{2}$	$\frac{1}{2}$		
$\frac{1}{2}$	$-\frac{1}{2}$	$\pm\frac{\lvert\mathbf{k}\rvert}{\sqrt{-k^2}}\sum_j \frac{2j+1}{\sqrt{2}}\mathcal{D}^j(R)f^{V(-)}_{0+}\left[R\left(I, j=l\pm\frac{1}{2}\right)\right]d^j_{\frac{1}{2}-\frac{1}{2}}(\theta)$	$\pm\frac{\lvert\mathbf{k}\rvert}{\sqrt{-k^2}}\sum_j \frac{2j+1}{\sqrt{2}}\mathcal{D}^j(R)f^{V(+)}_{0+}\left[R\left(I, j=l\pm\frac{1}{2}\right)\right]d^j_{\frac{1}{2}-\frac{1}{2}}(\theta)$
$-\frac{1}{2}$	$-\frac{1}{2}$	$-\frac{\lvert\mathbf{k}\rvert}{\sqrt{-k^2}}\sum_j \frac{2j+1}{\sqrt{2}}\mathcal{D}^j(R)f^{V(-)}_{0+}\left[R\left(I, j=l\pm\frac{1}{2}\right)\right]d^j_{\frac{1}{2}\frac{1}{2}}(\theta)e^{i\phi}$	$-\frac{\lvert\mathbf{k}\rvert}{\sqrt{-k^2}}\sum_j \frac{2j+1}{\sqrt{2}}\mathcal{D}^j(R)f^{V(+)}_{0+}\left[R\left(I, j=l\pm\frac{1}{2}\right)\right]d^j_{\frac{1}{2}\frac{1}{2}}(\theta)e^{i\phi}$

TABLE IX. Isospin Clebsch-Gordan coefficients.

Channels	$C^{3/2}_{N\pi}$	$C^{1/2}_{N\pi}$
$ep \to ep\pi^0$	$\sqrt{\frac{2}{3}}$	$-\sqrt{\frac{1}{3}}$
$ep \to en\pi^+$	$-\sqrt{\frac{1}{3}}$	$-\sqrt{\frac{2}{3}}$

APPENDIX A: HELICITY AMPLITUDES FOR THE RESONANT INTERACTIONS

The helicity amplitudes of the vector current are given in Table VIII, where $f^V(R)$ is the production amplitude given in Eqs. (3)–(6) and $D(R)$ is the decay amplitude:

$$\mathcal{D}^j(R) = \langle N\pi, \lambda_2 | R\lambda_R\rangle = \sigma^D C^j_{N\pi}\sqrt{\chi_E}\kappa C^I_{N\pi} f_{\rm BW}, \quad \text{(A1)}$$

where $f_{\rm BW}(R)$ is the Breit-Wigner amplitude,

$$f_{\rm BW}(R) = \sqrt{\frac{\Gamma_R}{2\pi}}\left(\frac{1}{W - M_R + i\Gamma_R/2}\right), \quad \text{(A2)}$$

where

$$\Gamma_R = \Gamma_0(|\mathbf{q}(W)|/|\mathbf{q}(M_R)|)^{2l+1}, \quad \text{(A3)}$$

and

$$\kappa = \left(2\pi^2\frac{W^2}{M^2}\frac{2}{2j+1}\frac{1}{|\mathbf{q}|}\right)^{\frac{1}{2}}. \quad \text{(A4)}$$

Γ_0, M_R, σ^D, and χ_E are given in Table II and $C^I_{N\pi}$ are the isospin Clebsch-Gordan coefficients given in Table IX. The explicit forms of the $d^j_{\lambda,\mu}(\theta)$ functions for $j = l + \frac{1}{2}$ are

$$\begin{aligned}
d^j_{\frac{1}{2}\frac{1}{2}} &= (l+1)^{-1}\cos\tfrac{\theta}{2}(P'_{l+1} - P'_l),\\
d^j_{-\frac{1}{2}\frac{1}{2}} &= (l+1)^{-1}\sin\tfrac{\theta}{2}(P'_{l+1} + P'_l),\\
d^j_{\frac{1}{2}\frac{3}{2}} &= (l+1)^{-1}\sin\tfrac{\theta}{2}\left(\sqrt{\tfrac{l}{l+2}}P'_{l+1} + \sqrt{\tfrac{l+2}{l}}P'_l\right),\\
d^j_{-\frac{1}{2}\frac{3}{2}} &= (l+1)^{-1}\cos\tfrac{\theta}{2}\left(-\sqrt{\tfrac{l}{l+2}}P'_{l+1} + \sqrt{\tfrac{l+2}{l}}P'_l\right), \quad \text{(A5)}
\end{aligned}$$

where P_l are the Legendre polynomials and $P'_l = dP_l/d\cos\theta$.

APPENDIX B: HELICITY AMPLITUDES FOR THE NONRESONANT INTERACTIONS

The helicity amplitudes of the vector current are given in Table X, where

$$\mathscr{F}_i = K^V_i F_i \ (i = 1, \ldots, 6), \quad \text{(B1)}$$

where

$$\begin{aligned}
F_1 &= V_1 + (V_3 - V_4)(qk)/W_- + V_4 W_- - V_6 k^2/W_-,\\
F_2 &= -V_1 + (V_3 - V_4)(qk)/W_+ + V_4 W_+ - V_6 k^2/W_+,\\
F_3 &= V_3 - V_4 + V_{25}/W_+,\\
F_4 &= V_3 - V_4 - V_{25}/W_-,\\
F_5 &= V_1(W_+^2 - k^2)/2W - V_2(qk)(W_+^2 - k^2 + 2WW_-)/2W\\
&\quad + (V_3 - V_4)[W_+ q_0 - (qk)] + V_4(W_+^2 - k^2)W_-/2W\\
&\quad - V_5(qk)k_0 - V_6(W_+^2 - k^2)W_-/2W + q_0 V_{25},\\
F_6 &= -V_1(W_-^2 - k^2)/2W + V_2(qk)(W_+^2 - k^2 + 2WW_-)/2W\\
&\quad + (V_3 - V_4)[W_- q_0 - (qk)] + V_4(W_-^2 - k^2)W_+/2W\\
&\quad + V_5(qk)k_0 - V_6(W_-^2 - k^2)W_+/2W - q_0 V_{25}, \quad \text{(B2)}
\end{aligned}$$

and V_i $(i = 1, \ldots, 6)$ are presented in Table XI, where s, u, and t are invariant Mandelstam variables:

$$\begin{aligned}
s &= (p_2 + q)^2 = (p_1 + k)^2 = W^2,\\
t &= (k - q)^2, \ \text{and} \ u = (q - p_1)^2. \quad \text{(B3)}
\end{aligned}$$

TABLE X. Vector helicity amplitudes of nonresonant interaction.

λ_2	λ_1	$\tilde{F}^{e_L}_{\lambda_2\lambda_1}(\theta,\phi)$	$\tilde{F}^{e_R}_{\lambda_2\lambda_1}(\theta,\phi)$
$\frac{1}{2}$	$\frac{1}{2}$	$\frac{1}{\sqrt{2}}e^{-2i\phi}\sin\theta\cos\frac{\theta}{2}(\mathscr{F}_3 + \mathscr{F}_4)$	$-\sqrt{2}[\sin\frac{\theta}{2}(\mathscr{F}_1 + \mathscr{F}_2) + \frac{1}{2}\sin\theta\cos\frac{\theta}{2}(\mathscr{F}_3 + \mathscr{F}_4)]$
$-\frac{1}{2}$	$\frac{1}{2}$	$-\frac{1}{\sqrt{2}}e^{-i\phi}\sin\theta\sin\frac{\theta}{2}(\mathscr{F}_3 - \mathscr{F}_4)$	$-\sqrt{2}e^{i\phi}[\cos\frac{\theta}{2}(\mathscr{F}_1 - \mathscr{F}_2) - \frac{1}{2}\sin\theta\sin\frac{\theta}{2}(\mathscr{F}_3 - \mathscr{F}_4)]$
$\frac{1}{2}$	$-\frac{1}{2}$	$\sqrt{2}e^{-i\phi}\big[\cos\frac{\theta}{2}(\mathscr{F}_1 - \mathscr{F}_2) - \frac{1}{2}\sin\theta\sin\frac{\theta}{2}(\mathscr{F}_3 - \mathscr{F}_4)\big]$	$\frac{1}{\sqrt{2}}e^{i\phi}\sin\theta\sin\frac{\theta}{2}(\mathscr{F}_3 - \mathscr{F}_4)$
$-\frac{1}{2}$	$-\frac{1}{2}$	$-\sqrt{2}\big[\sin\frac{\theta}{2}(\mathscr{F}_1 + \mathscr{F}_2) + \frac{1}{2}\sin\theta\cos\frac{\theta}{2}(\mathscr{F}_3 + \mathscr{F}_4)\big]$	$\frac{1}{\sqrt{2}}e^{2i\phi}\sin\theta\cos\frac{\theta}{2}(\mathscr{F}_3 + \mathscr{F}_4)$
		$\tilde{F}^{e_-}_{\lambda_2\lambda_1}(\theta,\phi)$	$\tilde{F}^{e_+}_{\lambda_2\lambda_1}(\theta,\phi)$
$\frac{1}{2}$	$\frac{1}{2}$	$e^{-i\phi}\cos\frac{\theta}{2}\frac{1}{C_-}\big(k_0\epsilon^0_L - |\mathbf{k}|\epsilon^3_L\big)(\mathscr{F}_5 + \mathscr{F}_6)$	$e^{-i\phi}\cos\frac{\theta}{2}\frac{1}{C_+}\big(k_0\epsilon^0_R - |\mathbf{k}|\epsilon^3_R\big)(\mathscr{F}_5 + \mathscr{F}_6)$
$-\frac{1}{2}$	$\frac{1}{2}$	$-\sin\frac{\theta}{2}\frac{1}{C_-}\big(k_0\epsilon^0_L - |\mathbf{k}|\epsilon^3_L\big)(\mathscr{F}_5 - \mathscr{F}_6)$	$-\sin\frac{\theta}{2}\frac{1}{C_+}\big(k_0\epsilon^0_R - |\mathbf{k}|\epsilon^3_R\big)(\mathscr{F}_5 - \mathscr{F}_6)$
$\frac{1}{2}$	$-\frac{1}{2}$	$-\sin\frac{\theta}{2}\frac{1}{C_-}\big(k_0\epsilon^0_L - |\mathbf{k}|\epsilon^3_L\big)(\mathscr{F}_5 - \mathscr{F}_6)$	$-\sin\frac{\theta}{2}\frac{1}{C_+}\big(k_0\epsilon^0_R - |\mathbf{k}|\epsilon^3_R\big)(\mathscr{F}_5 - \mathscr{F}_6)$
$-\frac{1}{2}$	$-\frac{1}{2}$	$-e^{i\phi}\cos\frac{\theta}{2}\frac{1}{C_-}\big(k_0\epsilon^0_L - |\mathbf{k}|\epsilon^3_L\big)(\mathscr{F}_5 + \mathscr{F}_6)$	$-e^{i\phi}\cos\frac{\theta}{2}\frac{1}{C_+}\big(k_0\epsilon^0_R - |\mathbf{k}|\epsilon^3_R\big)(\mathscr{F}_5 + \mathscr{F}_6)$

TABLE XI. Vector invariant amplitudes.

Amplitude	$e+p\to ep\pi^0$	$e+p\to en\pi^+$
V_1	$\frac{Mg_A}{f_\pi}\left(\frac{1}{s-M^2}+\frac{1}{u-M^2}\right)F_1(k^2)+\frac{g_A}{Mf_\pi}\mu_V F_2(k^2)$	$\sqrt{2}\frac{Mg_A}{f_\pi}\left(\frac{1}{s-M^2}-\frac{1}{u-M^2}\right)F_1(k^2)$
V_2	$\frac{Mg_A}{f_\pi}\frac{1}{qk}\left(\frac{1}{s-M^2}+\frac{1}{u-M^2}\right)F_1(k^2)$	$\sqrt{2}\frac{Mg_A}{f_\pi}\frac{1}{qk}\left(\frac{1}{s-M^2}-\frac{1}{u-M^2}\right)F_1(k^2)$
V_3	$-\frac{g_A}{2f_\pi}\left(\frac{1}{s-M^2}-\frac{1}{u-M^2}\right)F_2(k^2)$	$-\frac{g_A}{\sqrt{2}f_\pi}\left(\frac{1}{s-M^2}+\frac{1}{u-M^2}\right)F_2(k^2)$
V_4	$-\frac{g_A}{2f_\pi}\left(\frac{1}{s-M^2}+\frac{1}{u-M^2}\right)F_2(k^2)$	$-\frac{g_A}{\sqrt{2}f_\pi}\left(\frac{1}{s-M^2}-\frac{1}{u-M^2}\right)F_2(k^2)$
V_5	0	$-\sqrt{2}\frac{g_A}{f_\pi}\frac{1}{qk}\frac{1}{t-m_\pi^2}F_1(k^2)$

K_i^V are given in Ref. [3]:

$$\begin{aligned} K_1^V &= W_- O_{1+}, \quad K_4^V = q^2 W_+ O_{2-}, \\ K_2^V &= W_+ O_{1-}, \quad K_5^V = 1/O_{2+}, \\ K_3^V &= q^2 W_+ O_{2-}, \quad K_6^V = 1/O_{2-}, \end{aligned} \tag{B4}$$

where

$$\begin{aligned} O_{1\pm} &= [(W_\pm^2 - k^2)(W_\pm^2 - m_\pi^2)]^{\frac{1}{2}}/2W, \\ O_{2\pm} &= [(W_\pm^2 - k^2)/(W_\pm^2 - m_\pi^2)]^{\frac{1}{2}}. \end{aligned} \tag{B5}$$

[1] M. Kabirnezhad, Phys. Rev. D **97**, 013002 (2018).
[2] M. Kabirnezhad, Phys. Rev. D **102**, 053009 (2020).
[3] S. L. Adler, Ann. Phys. **50**, 189 (1968).
[4] D. Rein and L. M. Sehgal, Ann. Phys. **133**, 79 (1981).
[5] D. Rein, Z. Phys. C **35**, 43 (1987).
[6] T. Sato, D. Uno, and T. S. H. Lee, Phys. Rev. C **67**, 065201 (2003).
[7] E. Hernandez, J. Nieves, and M. Valverde, Phys. Rev. D **76**, 033005 (2007).
[8] A. Mariano, C. Barbero, and G. Lopez Castro, Nucl. Phys. A **849**, 218 (2011).
[9] S. X. Nakamura, H. Kamano, and T. Sato, Phys. Rev. D **92**, 074024 (2015).
[10] M. Rafi Alam, M. Sajjad Athar, S. Chauhan, and S. K. Singh, Int. J. Mod. Phys. E **25**, 1650010 (2016).
[11] R. González-Jiménez, N. Jachowicz, K. Niewczas, J. Nys, V. Pandey, T. Van Cuyck, and N. Van Dessel, Phys. Rev. D **95**, 113007 (2017).
[12] D.-L. Yao, L. Alvarez-Ruso, A. N. H. Blin, and M. J. Vicente Vacas, Phys. Rev. D **98**, 076004 (2018).
[13] D.-L. Yao, L. Alvarez-Ruso, and M. J. Vicente Vacas, Phys. Lett. B **794**, 109 (2019).
[14] M. Kabirnezhad, JPS Conf. Proc. **12**, 010043 (2016).
[15] M. Kabirnezhad, J. Phys.: Conf. Ser. **888**, 012122 (2017).
[16] M. Kabirnezhad, PoS **NOW2018**, 033 (2019).
[17] T. Sato, Eur. Phys. J. Spec. Top. **230**, 4409 (2021).
[18] R. González-Jiménez, A. Nikolakopoulos, N. Jachowicz, and J. M. Udías, Phys. Rev. C **100**, 045501 (2019).
[19] J. E. Amaro, M. B. Barbaro, J. A. Caballero, R. González-Jiménez, G. D. Megias, and I. Ruiz Simo, J. Phys. G: Nucl. Part. Phys. **47**, 124001 (2020).
[20] T. Franco-Munoz, R. González-Jiménez, and J. M. Udías, arXiv:2203.09996.
[21] A. Nikolakopoulos, R. González-Jiménez, N. Jachowicz, and J. M. Udías, arXiv:2210.12144.
[22] M. Sajjad Athar, A. Fatima, and S. K. Singh, Prog. Part. Nucl. Phys. **129**, 104019 (2023).
[23] G. Vereshkov and N. Volchanskiy, Phys. Rev. D **76**, 073007 (2007).
[24] O. Lalakulich, N. Jachowicz, C. Praet, and J. Ryckebusch, Phys. Rev. C **79**, 015206 (2009).
[25] M. S. Athar and J. G. Morfín, J. Phys. G: Nucl. Part. Phys. **48**, 034001 (2021).
[26] O. Lalakulich, E. A. Paschos, and G. Piranishvili, Phys. Rev. D **74**, 014009 (2006).
[27] P. Stoler, Phys. Rep. **226**, 103 (1993).
[28] E. L. Lomon, Phys. Rev. C **66**, 045501 (2002).
[29] M. Guidal, J. M. Laget, and M. Vanderhaeghen, Nucl. Phys. A **627**, 645 (1997).
[30] M. M. Kaskulov and U. Mosel, Phys. Rev. C **81**, 045202 (2010).
[31] K. Joo*et al.* (CLAS Collaboration), Phys. Rev. Lett. **88**, 122001 (2002).
[32] H. Egiyan *et al.* (CLAS Collaboration), Phys. Rev. C **73**, 025204 (2006).
[33] I. G. Aznauryan *et al.* (CLAS Collaboration), Phys. Rev. C **80**, 055203 (2009).
[34] M. Ungaro *et al.* (CLAS Collaboration), Phys. Rev. Lett. **97**, 112003 (2006).
[35] K. Park *et al.* (CLAS Collaboration), Phys. Rev. C **77**, 015208 (2008).
[36] A. D. Carlson *et al.*, Nucl. Data Sheets **110**, 3215 (2009).
[37] https://userweb.jlab.org/~lcsmith/EBAC/stf-tables/tables/ebac/readme.pdf.
[38] L. Alvarez-Ruso, L. S. Geng, S. Hirenzaki, and M. J. Vicente Vacas, Phys. Rev. C **75**, 055501 (2007); **80**, 019906(E) (2009).
[39] D. Drechsel, S. S. Kamalov, and L. Tiator, Eur. Phys. J. A **34**, 69 (2007).
[40] H. Kamano, S. X. Nakamura, T. S. H. Lee, and T. Sato, Phys. Rev. C **88**, 035209 (2013).
[41] H. Kamano, S. X. Nakamura, T. S. H. Lee, and T. Sato, Phys. Rev. C **94**, 015201 (2016).
[42] https://www.phy.anl.gov/theory/research/anl-osaka-pwa/.
[43] https://www.rcnp.osaka-u.ac.jp/~anl-osk/.
[44] https://maid.kph.uni-mainz.de/maid2007/.